Materials Today Communications 56 (2026) 116119

Contents lists available at ScienceDirect

Materials Today Communications

journal homepage: www.elsevier.com/locate/mtcomm

# A quad-band terahertz plasmonic sensor based on a graphene metamaterial absorber with symmetric coupled multi-strip resonators

Mohadese Imani, Seyed Amin Khatami, Shiva Khani, Mohammad Danaie *

*Electrical and Computer Engineering Faculty, Semnan University, Semnan, Iran*

ARTICLE INFO

*Keywords:*
Graphene Plasmonic Resonator
Quad-Band Sensing
Terahertz Metamaterial Absorber
Cross-Shaped Graphene Array

ABSTRACT

In this paper, a four-band refractive index sensor is introduced, composed of an interwoven array of graphene nanostrips with attached appendages. The proposed design highlights the significance of graphene as a fundamental material in the development of plasmonic sensors operating in the terahertz (THz) domain and demonstrates its efficiency in emerging optoelectronic applications. The sensor can simultaneously exhibit the Surface Plasmon Resonance (SPR) phenomenon across four distinct frequency bands, leading to a significant enhancement in detection sensitivity. The proposed structure consists of four layers, sequentially arranged as gold, $SiO_2$, graphene, and the analyte material. The sensitivity and Quality Factor are reported as 1314 GHz/RIU and 33.708, respectively. For analysis, the FEM-based frequency-domain solver in CST Microwave Studio and Coupled Mode Theory (CMT) were utilized. The sensor displays four resonance peaks at frequencies of 5.29, 6.66, 8.02, and 11.44 THz, with corresponding absorptions of 97.1%, 96.1%, 99.9%, and 99.2%, respectively. Given its ability to accurately distinguish between frequencies and the stable resonance behavior observed in the numerical analysis, this sensor may be considered a promising candidate for refractive index sensing applications, particularly within the terahertz frequency range.

## 1. Introduction

Among various frequency regions, the terahertz band has gained a special position due to its distinctive characteristics and has found wide-ranging applications. The most important of these features include its non-ionizing radiation nature, good coherence, high safety, considerable bandwidth, and desirable spectral resolution [1–5]. These properties have made terahertz waves a focal point in many scientific and technological fields as an efficient and reliable option. Recent advancements in multilayer SPR sensors have highlighted the critical role of material composition and layer thickness in enhancing sensing performance. For instance, it has been demonstrated that the precise calibration of metallic layers, such as Ag and Au combined with TlBr, can optimize the trade-off between sensitivity and Figure of Merit (FoM), achieving sensitivities up to 368.38 °/RIU [6]. Similarly, the integration of 2D materials like MXene and $TaS_2$ has shown great promise in improving field confinement and molecular attachment due to their high optical tunability and biocompatibility [7]. The proposed sensor, utilizing a Gold/$SiO_2$/Graphene architecture, leverages the unique potentials of graphene in the THz regime. The use of graphene in this regime allows for dynamic tuning of the resonance characteristics via chemical potential adjustments, providing a versatile platform that enhances sensing performance beyond the limits of static multilayer designs.

In the telecommunications and electronics industries, particularly at high-frequency regimes, a wide range of functional devices play essential roles, including sensors [8,9], filters [10–13], switches [14–17], antennas [18,19], neural networks [20,21], and absorbers [22–24]. To date, most reported absorber designs have focused on achieving perfect absorption at one or two discrete wavelengths. However, such narrowband designs are often inadequate for practical sensing applications, where simultaneous detection at multiple frequencies is desirable. Consequently, multiband absorbers have attracted increasing attention. These structures are typically realized by integrating different nanoribbon geometries within a single architecture, thereby providing multiple resonant absorption bands that better satisfy the requirements of modern sensing technologies [25,26].

In recent years, metamaterials (MMs) have emerged as an important

* Corresponding author.
*E-mail addresses:* mohadese.imani@semnan.ac.ir (M. Imani), aminkhatami@semnan.ac.ir (S.A. Khatami), shiva.khani@semnan.ac.ir (S. Khani), danaie@semnan.ac.ir (M. Danaie).

https://doi.org/10.1016/j.mtcomm.2026.116119
Received 8 June 2026; Received in revised form 20 August 2026; Accepted 8 September 2026
Available online 10 September 2026

research area because of their extraordinary electromagnetic properties, which are unattainable in naturally occurring materials. Metamaterials consist of periodically arranged subwavelength structural elements, commonly referred to as unit cells, whose geometry determines the overall electromagnetic response. Through appropriate engineering of these unit cells, metamaterials can exhibit unconventional electromagnetic characteristics and enable phenomena that are impossible to achieve using conventional materials [27]. Among these structures, metamaterial perfect absorbers (MPAs) have received considerable attention owing to their exceptional electromagnetic properties, including negative refractive index behavior under specific operating conditions [28–31]. In addition to their superior absorption performance, MPAs have demonstrated significant potential as high-sensitivity refractive index (RI) sensors, enabling the detection of subtle variations in the surrounding dielectric environment [32–35].

Graphene, a two-dimensional material composed of a single layer of carbon atoms arranged in a hexagonal honeycomb lattice, has attracted tremendous research interest because of its extraordinary electrical, optical, thermal, and mechanical properties [36,37]. Owing to its atomic-scale thickness, exceptionally high electrical and thermal conductivity, excellent mechanical strength, and remarkable optical characteristics, graphene has become one of the most promising materials for next-generation photonic and optoelectronic devices [38]. In particular, graphene plays a pivotal role in the development of terahertz (THz) technologies due to its electrically tunable surface conductivity and strong interaction with THz electromagnetic waves. Consequently, graphene has been widely employed in numerous THz applications, including antennas [39,40], absorbers [41–46], biosensors [47–50], and various sensing platforms [51–54].

Recent advances in graphene-based absorbers have led to the development of multi-band and reconfigurable structures with discrete and tunable resonance peaks [55–57]. In parallel, broadband and narrowband absorber designs have also been extensively investigated to achieve strong absorption over different frequency ranges [58–61]. Additional broadband configurations have further expanded the achievable performance of these structures [62]. These distinctive properties have enabled graphene-based metastructures to attract significant attention for enhanced light-matter interactions [63]. Beyond absorber-based platforms, graphene has also been employed in other sensing architectures, such as ionic liquid-gated FET sensors [64]. Finally, these capabilities have provided great potential for highly sensitive sensing applications, including refractive index and selective sensing [65–67].

Through careful structural optimization and the exploitation of graphene's tunable electronic properties, these absorbers have demonstrated significantly improved absorption efficiency, spectral selectivity, and operational flexibility, making them promising candidates for advanced sensing, imaging, and communication systems.

In this study, a multiband sensor composed of graphene ribbons is proposed. These ribbons are placed on a gold layer and a $SiO_2$ dielectric layer. The FEM-based frequency-domain simulations performed in CST Microwave Studio demonstrate that the sensor exhibits four resonance peaks at 5.29, 6.66, 8.02, and 11.44 THz, with corresponding absorption levels of 97.1%, 96.1%, 99.9%, and 99.2%, respectively. The sensitivity and Q-factor were obtained as 1314 GHz/RIU and 33.708, respectively. This sensor is capable of effectively distinguishing between different frequencies and demonstrates strong performance in detection. The following sections present the structure of this study: The details related to graphene conductivity are presented in Section 2. The sensor structure and its corresponding settings are provided in Section 3. The results are presented in Section 4. Section 5 examines the performance of the sensor as a refractive-index sensor. The final section contains the conclusion.

## 2. Theoretical analysis

The surface conductivity of graphene, denoted as $\sigma_g(\omega, \mu_c, \tau, T)$, is influenced by four key factors: the wave frequency ($\omega$), the chemical potential ($\mu_c$), the electron relaxation time ($\tau$), and the material's temperature ($T$). To obtain an accurate expression for this conductivity, the Kubo formalism is employed. In general, graphene's conductivity consists of two main components. The first arises from electronic transitions occurring within a single energy band (intra-band), while the second originates from transitions taking place between different energy bands (inter-band). The complete analysis and formulation of these contributions are presented in Eqs. 1 through 3. The Kubo formalism for graphene's surface conductivity is correctly expressed as the sum of intra-band and inter-band contributions:

$$\sigma_g(\omega, \mu_c, \Gamma, T) = \sigma_{\text{intra}} + \sigma_{\text{inter}} \tag{1}$$

The intra-band conductivity, which dominates in the terahertz frequency range, is given by:

$$\sigma_{\text{intra}}(\omega, \mu_c, T) = \frac{iq_e^2 k_B T}{\pi(\omega + i2\Gamma)\hbar^2}\left(\frac{\mu_c}{k_B T} + 2\ln\left(e^{-\frac{\mu_c}{k_B T}} + 1\right)\right) \tag{2}$$

The inter-band conductivity, which becomes significant at higher frequencies (typically above ~10 THz), is expressed as:

$$\sigma_{\text{inter}} = \frac{iqe^2}{4\pi\hbar}\left(\frac{2|\mu_c|}{(\omega + i2\Gamma)\hbar} + \frac{(\omega + i2\Gamma)\hbar}{2|\mu_c|}\right) \tag{3}$$

It is important to note that in the terahertz regime (4–12 THz) and for the selected chemical potential values (μc = 0.6–0.9 eV), the intra-band contribution dominates the conductivity response, as the inter-band transitions are suppressed due to Pauli blocking.This justifies the use of the simplified intra-band model for our analysis [68,69].

Here, we have $e = 1.6 \times 10^{-19}$C as the electron charge, $k_B = 8.617 \times 10^{-5}$eV.K$^{-1}$ as the Boltzmann constant, and $\hbar = 6.582 \times 10^{-16}$eV.s as the approximate Planck constant.

Subsequently, the relationship between tau ($\tau$) and gamma ($\Gamma$) is defined as follows:

$$\Gamma = \frac{1}{2\tau} \tag{4}$$

Γ (Gamma): Represents the phenomenological electron scattering rate, which accounts for the damping of electron oscillations due to scattering events. This parameter appears directly in the denominator of the conductivity formula as (ω+i2Γ).

τ (Tau): Represents the electron relaxation time, which is the average time between scattering events.

Fig. 1 illustrates the relationship between graphene's chemical potential and the variation of the real and imaginary components of its electrical conductivity, providing a more comprehensive understanding of its electromagnetic behavior. As the figure suggests, adjusting the frequency leads to consistent and recognizable shifts in both parts of the conductivity response.

According to the transmission line theory, the absorption coefficient ($A$) can be expressed in terms of the relative impedance $Z_r$as:

$$\boldsymbol{Z = Z_0 = \sqrt{\frac{\mu_0}{\epsilon_0}} \approx 377\Omega} \tag{5}$$

$$\boldsymbol{A = 1 - R = 1 - \left|\frac{Z - Z_0}{Z + Z_0}\right|^2 = 1 - \left|\frac{Z_r - 1}{Z_r + 1}\right|^2} \tag{6}$$

where $Z_0$represents the impedance of free space, and $\mu_0$and $\epsilon_0$are the magnetic permeability and dielectric constant in free space, respectively. The relative impedance $Z_r = Z/Z_0$is retrieved from the $S$-parameters using the following formula:

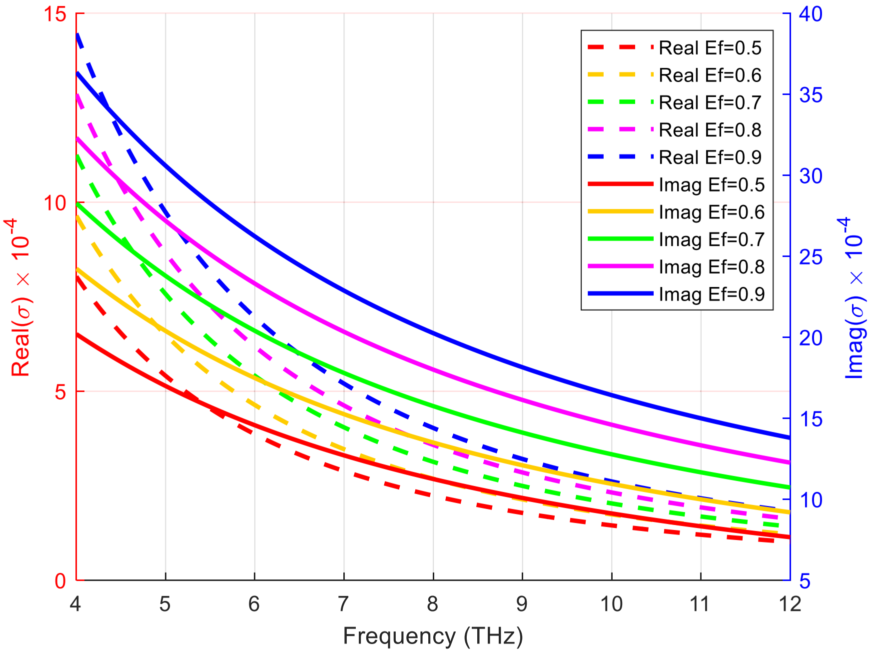


**Fig. 1.** Graphene conductivity Real part and imaginary part [67].

$$Z_r = \pm\sqrt{\frac{(1+S_{11})^2 - S_{21}^2}{(1-S_{11})^2 - S_{21}^2}} \quad (7)$$

Since our proposed absorber utilizes a continuous metallic ground plane at the bottom, the transmission coefficient is zero ($S_{21} = 0$). Consequently, this relation simplifies to:

$$Z_r = \frac{1+S_{11}}{1-S_{11}} \quad (8)$$

To achieve perfect absorption ($A\rightarrow1$), the equivalent impedance of the metasurface must match the free-space impedance, which theoretically requires $\Re(Z_r)\rightarrow1$and $\Im(Z_r)\rightarrow0$at the absorption peaks. [2]

As shown in Fig. 2, the real part $\mathrm{Re}(Z_r)$is significantly near 1 and the imaginary part $\mathrm{Im}(Z_r)$vanishes at the four resonant frequencies (5.29, 6.66, 8.02, and 11.44 THz). This impedance matching performance physically justifies the near-perfect multi-band absorption of the proposed structure.

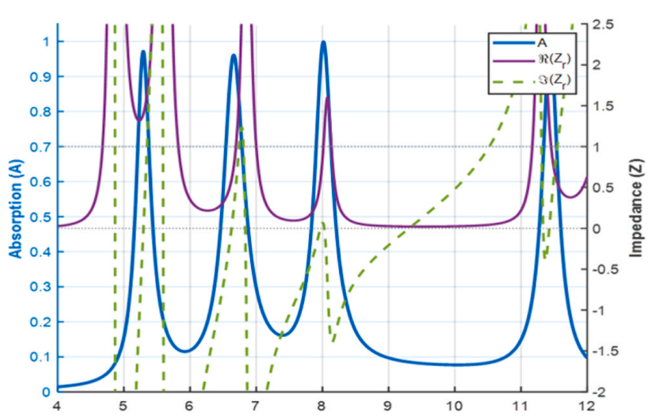


**Fig. 2.** Absorption spectrum and relative impedance ($\mathrm{Re}(Z_r)$ and $\mathrm{Im}(Z_r)$) of the proposed absorber. [2].

## 3. Absorber theory and design

Schematic illustration of the proposed structure four-band sensor is shown in Fig. 3. The graphene-based sensor consists of three layers, where the bottom layer is a gold metallic sheet with an electrical conductivity of $\sigma = 4.56\times10^7$ S/m. The middle layer is made of silicon dioxide ($SiO_2$) with a dielectric constant of $\varepsilon_d = 3.9$. Graphene strips constitute the top layer— four peripheral graphene ribbons with attached extensions, along with two coupled central graphene ribbons, each having a thickness of 0.35 nm. On top of these layers, a 2 μm thick analyte layer is placed. In this section, the geometric parameters are determined as follows: $HAu = 0.2$ μm, $HSiO2 = 4$ μm, V1 = 0.4μm, V2 =

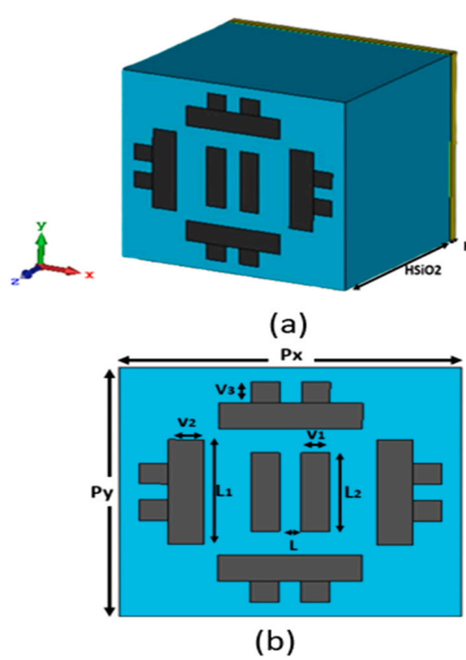


**Fig. 3.** (a) Perspective representation of the designed THz absorber. (b) Its X–Y view.

0.5 µm, V3 = 0.4µm, L= 0.15 µm, L1 = 2µm, L2 = 1.5µm, respectively. The proposed structure's period is PX = PY = 4.75 µm. To perform the electromagnetic computations, the frequency-domain solver in CST software was utilized. To implement the periodic array configuration of the structure, Floquet port boundary conditions were applied along the *x*- and *y*-axes. Furthermore, in the wave propagation direction (*z*-axis), open-space boundary conditions were simulated using perfectly matched layers (PML) to guarantee the accuracy of the results by eliminating unwanted reflections. Detailed simulation configurations are provided below:

The structure was discretized using a surface-based tetrahedral meshing scheme in CST Studio Suite 2025. The mesh density was defined with 10 cells per maximum model box edge, resulting in a final mesh count of 27,400 tetrahedrons. To ensure numerical stability and accuracy, the mesh quality was maintained at an average of 0.775 (with a maximum of 0.999). The minimum edge length was refined to 0.02 $\mu$ µm, which is sufficiently small to resolve the localized field enhancements at the graphene interfaces. These statistics confirm that the mesh resolution is adequate to capture the plasmonic resonance effects with high fidelity and stable convergence.

## 4. Results and analysis

The operation of the proposed sensor was evaluated using frequency-domain simulations in the CST Microwave Studio environment, with the corresponding results presented in Fig. 4. The absorption spectra for configurations (d), (e), and (f) are presented. Figure (a) consists of four graphene ribbons exhibiting a single resonance peak at 5.50 THz. As depicted in Figure (b), a structure formed by four outer graphene ribbons and two coupled ribbons at the center gives rise to two distinct absorption peaks located at 5.53 THz and 6.82 THz. Meanwhile, the design illustrated in Figure (c) supports four resonance modes at 5.29 THz ($f_1$), 6.66 THz ($f_2$), 8.02 THz ($f_3$), and 11.44 THz ($f_4$), with absorption levels reaching 97.1%, 96.1%, 99.9%, and 99.2%, respectively.

This figure shows the distribution of the vertical component of the electric field (Ez) at the absorption peak. As depicted in Fig. 5(a), at the approximate resonance frequency of 5.29 THz, the electric field is mainly dispersed over the lateral strips and their extended appendages. When the resonance shifts to 6.66 THz, the field becomes more concentrated in the central region of the coupled strip structure. At the 8.02 THz resonance, most of the electric field intensity accumulates around the graphene appendage regions. Finally, at 11.44 THz, the field pattern shifts upward and downward along the strips and their corresponding extensions. Fig. 5(e) through (h) illustrate the distribution of the vertical component of the magnetic field ($H_z$) at the absorption peaks. As depicted in Fig. 5(e), at the approximate resonance frequency of 5.29 THz, the magnetic field is mainly dispersed over the lateral strips and their extended appendages. When the resonance shifts to 6.66 THz, the field becomes more concentrated in the central region of the coupled structure. At the 8.02 THz resonance, most of the magnetic field intensity accumulates around the graphene appendage regions. Finally, at 11.44 THz, the field pattern shifts upward and downward along the strips and their corresponding extensions. To further elucidate the physical origin of the four absorption peaks, the spatial distributions of the electric field (|Ez|) and magnetic field (|Hz|) are illustrated in Fig. 5. At the first resonance (5.29 THz), the electric field is primarily localized at the outer edges of the side strips, indicating a fundamental dipolar resonance of the entire structure. For the second peak at 6.66 THz, a strong enhancement of both electric and magnetic fields is observed within the central coupled resonators, suggesting the excitation of symmetric coupled plasmonic modes. The third peak (8.02 THz) is characterized by field localization at the graphene appendages, confirming the role of the structural symmetry-breaking features. Finally, at 11.44 THz, the fields are highly confined at the sharp edges and small extremities, which is typical for higher-order plasmonic modes. The strong magnetic field concentration in the gaps between graphene elements at these frequencies indicates that the total absorption is a result

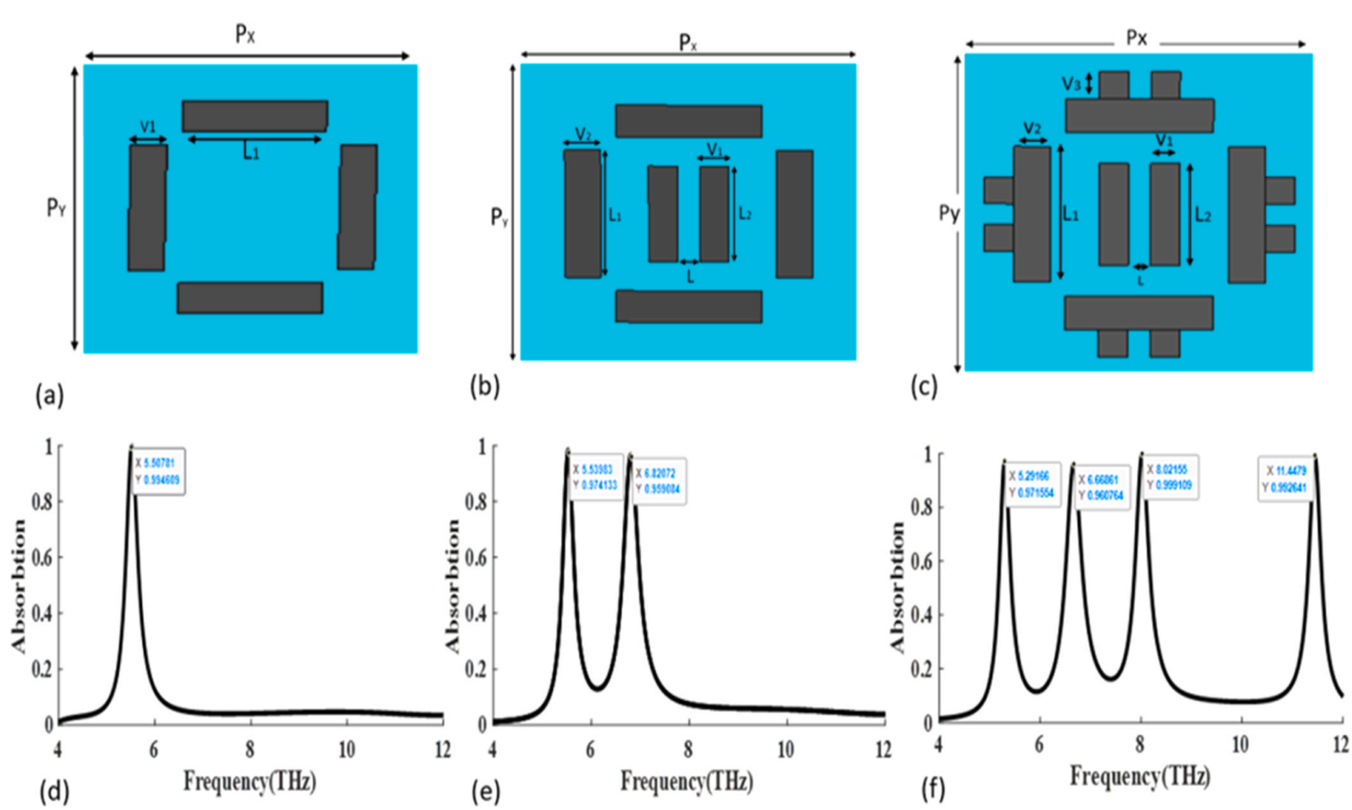


**Fig. 4.** (a) Structure 1, (b) structure 2, (c) structure 3, absorption spectrum of (d) structure 1, (e) structure 2, (f) structure 3.

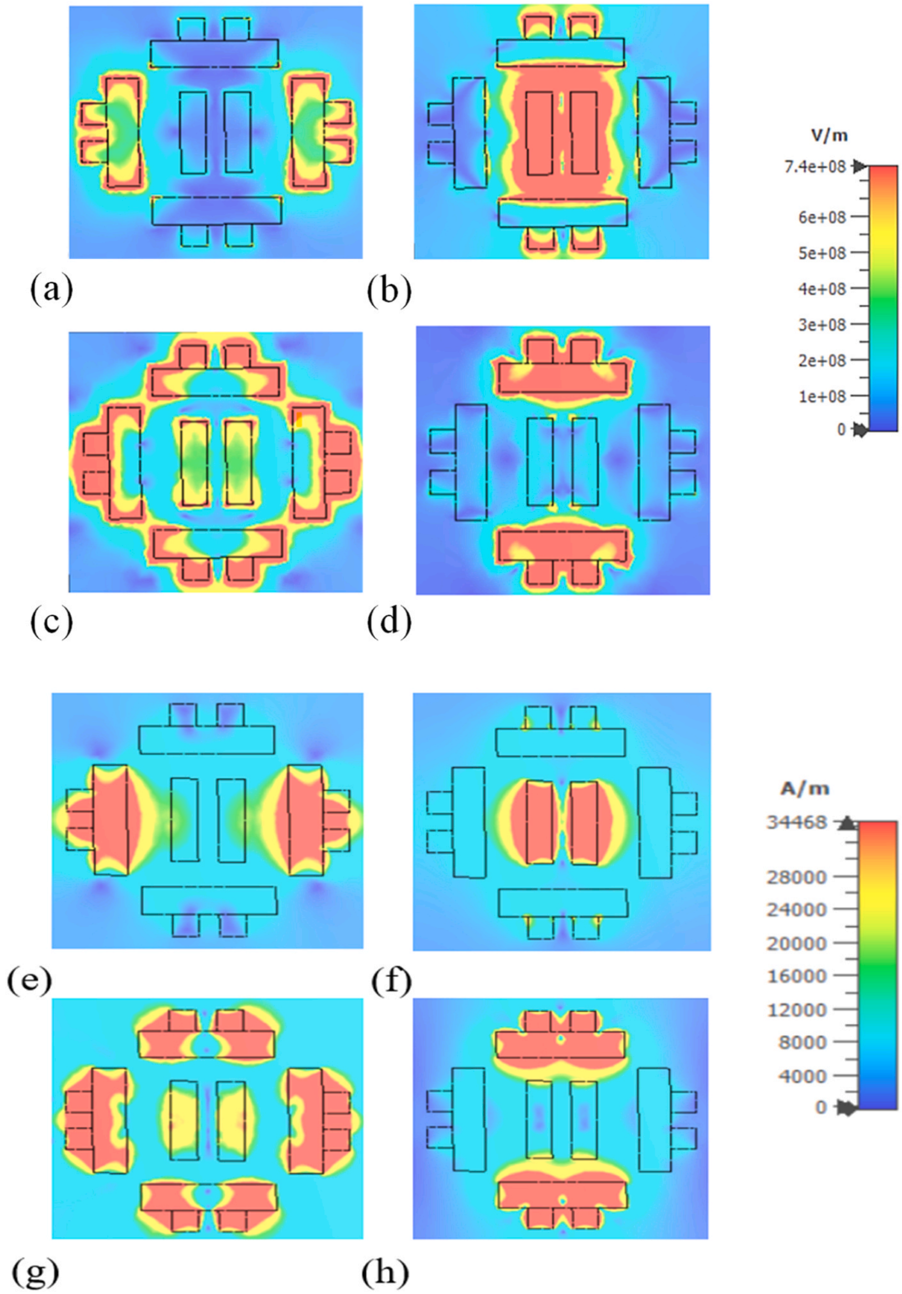


**Fig. 5.** The electric field distribution (|Ez|) in the proposed sensor structure at (a) 5.29 THz, (b) 6.66 THz, (c)8.02 THz, and (d) 11.44 THz. The magnetic field distribution (|*Hz*|) in the proposed sensor structure at (e) 5.29 THz, (f) 6.66 THz, (g) 8.02 THz, and (h) 11.44 THz.

of both electric and magnetic dipole resonances, leading to an efficient impedance matching with free space. Fig. 6 from a to d shows the parameter sweeps, based on the results, geometric parameters V1, V2, V3, and L were varied, yielding different absorption spectra. In Fig. 6(a), as the width of V1 increases from 0.3 to 0.5 micrometres, the resonant absorption peak frequencies $f_1$, $f_3$, and $f_4$ remain stable, while $f_2$ is shifted. With increasing V1, the frequency $f_2$ moves towards higher frequencies, and the absorption efficiency decreases. Consequently, the frequency $f_2$ corresponds to the coupled graphene strips in the centre. In Fig. 6(b), as L increases from 0.05 to 0.25 micrometres, only the frequency $f_2$ shifts towards higher frequencies, while the others remain constant. In Fig. 6(c), as V3 increases from 0.3 to 0.5 micrometres, the resonant absorption peak frequencies $f_1$, $f_2$, and $f_4$ are nearly constant, while the frequency $f_3$ shifts towards higher frequencies. Additionally, the absorption efficiency initially increases and then decreases. Frequency $f_3$ is related to the graphene appendages.

In Fig. 6(d), as V2 increases from 0.4 to 0.6 micrometres, the frequency $f_2$ remains nearly constant, while the others are shifted. Frequency $f_1$ moves towards higher frequencies, and the absorption efficiency increases. Frequency $f_3$ shifts to higher frequencies, while its absorption efficiency stays approximately unchanged. Similarly, $f_4$ shifts toward higher frequencies; however, its absorption efficiency first remains stable and then exhibits an increase.

Overall, Fig. 6 indicates a quasi-independent tuning behavior: $f_2$can be selectively tuned by $V_1$and L, and $f_3$is mainly controlled by $V_3$. However, varying $V_2$affects $f_1$, $f_3$, and $f_4$simultaneously, indicating mode coupling; therefore, the tuning is not fully independent for all four bands.

Among the parameters affecting graphene's surface conductivity, the relaxation time is particularly significant. In Fig. 7, the behavior of four

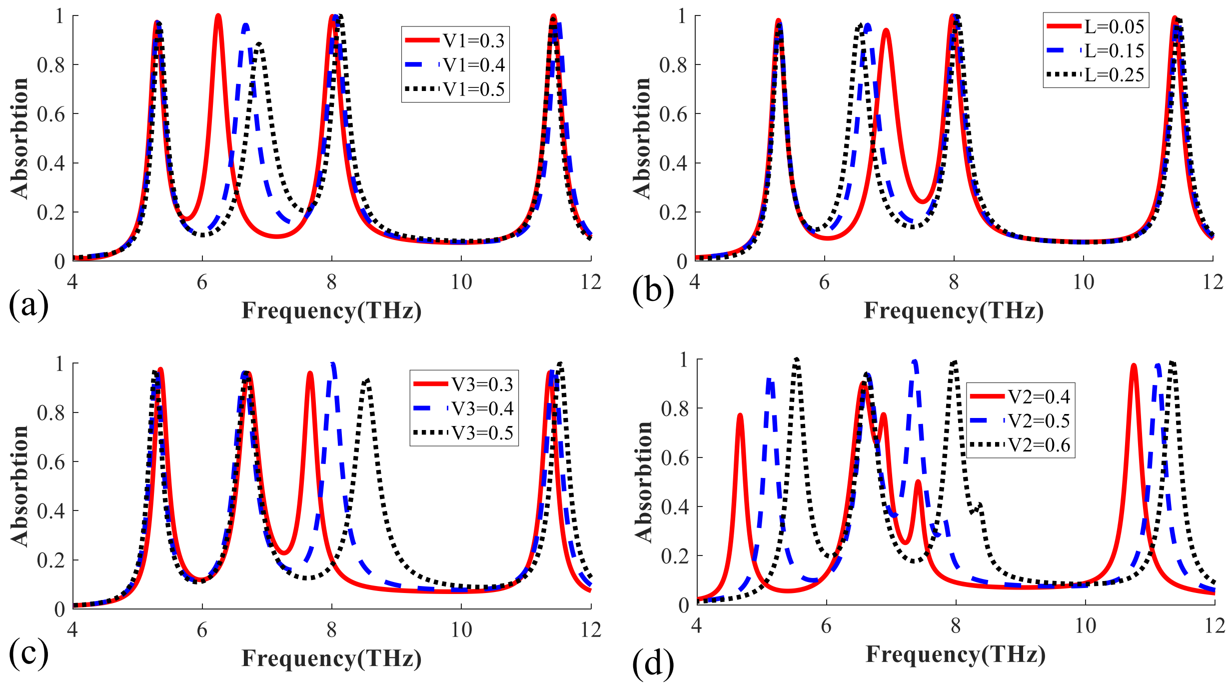


**Fig. 6.** Sensor absorption diagram: (a) when V1 is changed, (b) when L is changed, (c)when V3 is changed, (d) when V2 is changed.

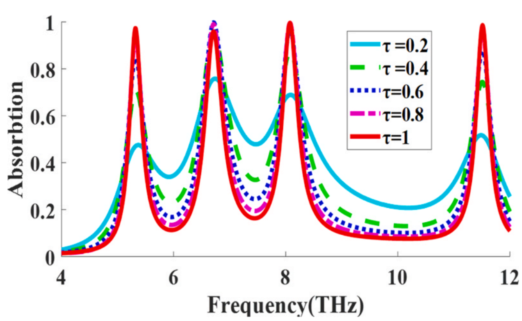


**Fig. 7.** Simulated absorption graph under different relaxation times (τ).

absorption modes is examined over a range from 0.2 to 1 picosecond. According to the observed results, Under the condition that the chemical potential is set to μc = 0.9, variations in the relaxation time do not lead to any shift in the absorption peak frequencies, and their positions remain unchanged. However, the bandwidth of these peaks gradually decreases, resulting in narrower peak shapes. Higher relaxation time (τ) means lower scattering rate (Γ), which leads to lower real part of conductivity and therefore lower ohmic losses. However, it also means higher imaginary part of conductivity, which enhances the plasmonic resonance quality (sharper and stronger resonance). This is why longer τ results in higher and narrower absorption peaks.

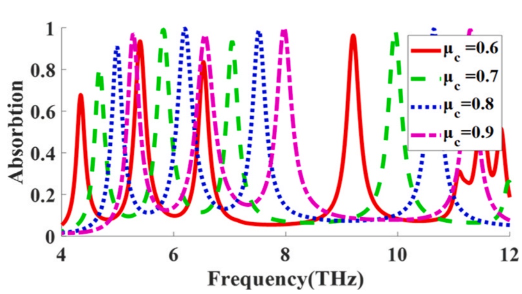


**Fig. 8.** Simulated absorption responses corresponding to different chemical potential ($\mu_c$) values.

As shown in the Fig. 8, raising $\mu_c$ from 0.6 eV to 0.9 eV improves the absorption performance of the graphene-based sensor. In addition, a higher chemical potential shifts the sensor's resonant frequencies toward the upper end of the frequency spectrum.

The fabrication methodology for the proposed graphene-based THz absorber is illustrated in the Fig. 9. The process commences with the synthesis of graphene layers on copper foil via chemical vapor deposition (CVD). To facilitate transfer onto the target substrate, a PMMA support layer is spin-coated onto the graphene, followed by the chemical etching of the copper foil using an $FeCl_3$ solution. Simultaneously, a gold back reflector and a dielectric $SiO_2$ spacer are deposited onto a $SiO_2$ wafer through sputtering. After the PMMA-graphene composite is transferred onto the prepared substrate, the PMMA layer is removed via acetone immersion. Finally, the desired geometry is defined on the graphene layer utilizing standard photolithography and reactive-ion etching (RIE) techniques

## 5. Refractive index sensor

The analyte, which represents the material under investigation, is positioned on the proposed structure, and its refractive index is systematically varied in a controlled manner. It has been observed that variations both increases and decreases in the analyte's refractive index lead to a displacement of the structure's absorption curve. This change signifies the appropriate performance and high sensing capability of the presented design. In Fig. 10, the behavior of the sensor's absorption spectrum can be observed for several different values of the analyte's refractive index

.

Graphene-based sensors used for monitoring the refractive index in the terahertz region are evaluated based on multiple criteria. Sensitivity, as the primary indicator in these evaluations, represents the sensor's response to variations in the refractive index of the surrounding environment. These variations are mainly accompanied by changes in resonance frequency or absorption intensity

$$S = \frac{\Delta f}{\Delta n} \quad (9)$$

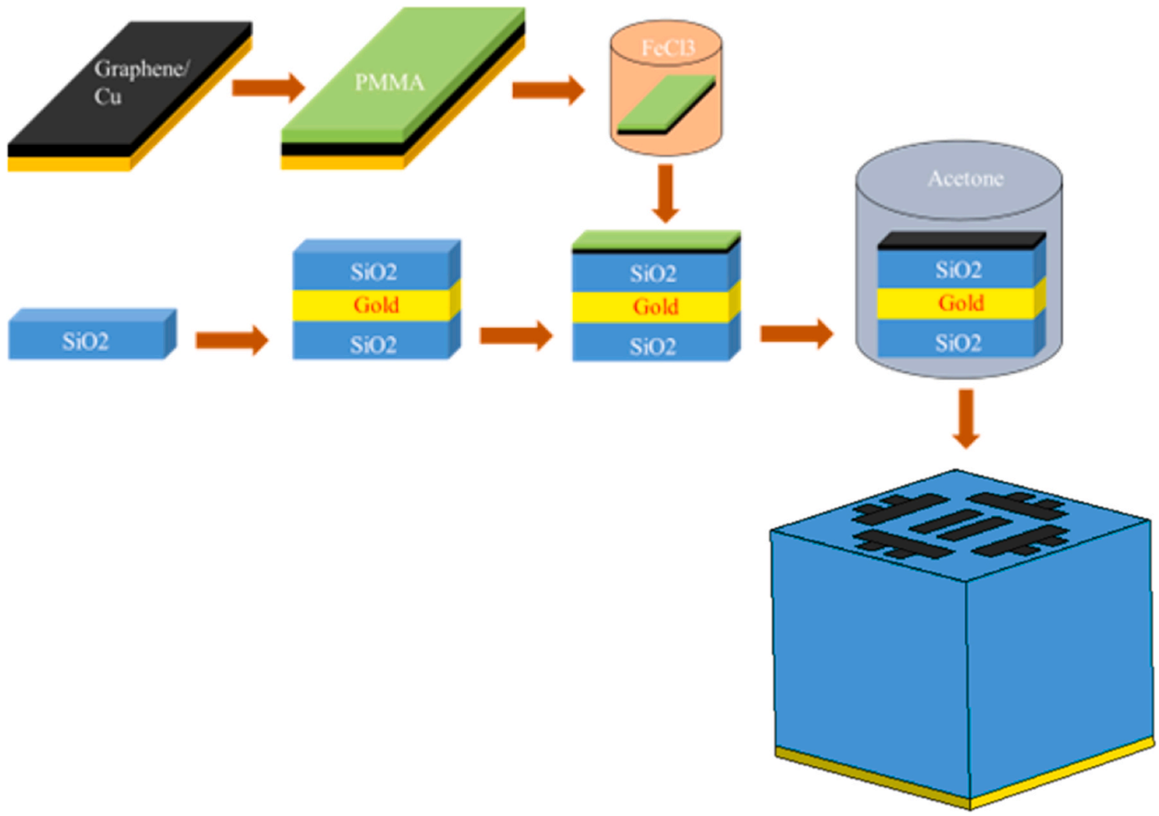


**Fig. 9.** The fabrication procedure for the proposed structure, adapted from [1].

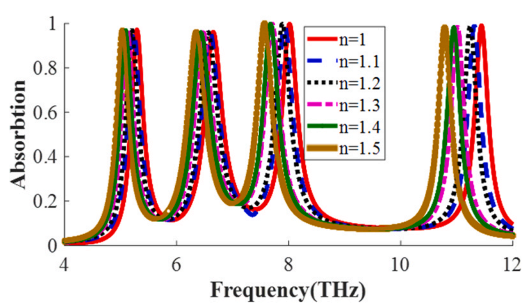


**Fig. 10.** The proposed sensor's absorption spectra demonstrate distinct patterns corresponding to different refractive indices of the analyte.

The Quality Factor (or Q factor) is a metric that indicates the degree of "purity" or "efficiency" of a resonant system (such as a resonator in a sensor or a resonant circuit). In simpler terms, this factor determines how much energy a resonant system can store compared to the energy dissipated in each oscillation cycle.

$$Q = \frac{f}{FWHM} \tag{10}$$

Figure of Merit (FOM), a combined metric, is used to comprehensively assess sensor performance. Typically defined as the ratio of sensitivity to resonance bandwidth, this index quantifies the sensor's ability to distinguish subtle signals (small changes in the measured parameter) from inherent device noise or uncertainty. In essence, a high FOM signifies a sensor that is both highly sensitive to minor variations and capable of resolving these changes with great precision and clarity, making it ideal for applications demanding accurate and reliable measurements.

$$FOM = \frac{S}{FWHM} \tag{11}$$

This figure shows how the absorption behavior evolves as the refractive index of the analyte changes from 1 to 1.5. With an increase in the refractive index, the absorption curve gradually shifts toward lower frequencies. The average FWHM for the four modes $f_1$, $f_2$, $f_3$, and $f_4$ are 288 GHz, 438 GHz, 396 GHz, and 328 GHz, respectively. The average sensitivities are S= 512 GHz/RIU for mode $f_1$, S= 592 GHz/RIU for mode $f_2$, S= 886 GHz/RIU for mode $f_3$, and S= 1314 GHz/RIU for mode $f_4$. Based on the results, the average figure of merit (FOM) is FOM= 1.776 ($RIU^{-1}$) for mode $f_1$, FOM= 1.349 ($RIU^{-1}$) for mode $f_2$, FOM= 2.247 ($RIU^{-1}$) for mode $f_3$, and FOM= 4.030 ($RIU^{-1}$) for mode $f_4$. Additionally, the average quality factor (Q) is Q= 17.906 for mode $f_1$, Q= 14.879 for mode $f_2$, Q= 19.685 for mode $f_3$, and Q= 33.875 for mode $f_4$. A detailed overview of the sensor's performance parameters is provided across Tables 1–4.

CMT provides a practical and intuitive way to explain how electromagnetic modes interact inside resonant structures. Within this approach, phenomena such as absorption, reflection, and transmission are explained based on the interaction and coupling between resonant modes and the incoming and outgoing fields. In this work, CMT is used

**Table 1**
Analysis of Sensor Response Variations in Mode 1 Induced by Refractive Index Changes.

| Refractive index | RPF | FWHM [THz] | Sensitivity [THz/ RIU] | FOM | Q-factor |
|---|---|---|---|---|---|
| 1 | 5.291 | 0.289 | - | - | 18.307 |
| 1.1 | 5.238 | 0.290 | 0.53 | 1.827 | 18.062 |
| 1.2 | 5.203 | 0.289 | 0.35 | 1.211 | 18.003 |
| 1.3 | 5.123 | 0.288 | 0.8 | 2.777 | 17.788 |
| 1.4 | 5.090 | 0.287 | 0.33 | 1.149 | 17.735 |
| 1.5 | 5.035 | 0.287 | 0.55 | 1.916 | 17.543 |

**Table 2**
Analysis of Sensor Response Variations in Mode **2** Induced by Refractive Index Changes.

| Refractive index | RPF | FWHM [THz] | Sensitivity [THz/RIU] | FOM | Q-factor |
|---|---|---|---|---|---|
| 1 | 6.625 | 0.435 | - | - | 15.291 |
| 1.1 | 6.603 | 0.437 | 0.49 | 1.121 | 15.109 |
| 1.2 | 6.566 | 0.437 | 0.37 | 0.846 | 15.025 |
| 1.3 | 6.476 | 0.439 | 0.9 | 2.050 | 14.751 |
| 1.4 | 6.435 | 0.44 | 0.41 | 0.931 | 14.625 |
| 1.5 | 6.356 | 0.439 | 0.79 | 1.799 | 14.478 |

**Table 3**
Analysis of Sensor Response Variations in Mode **3** Induced by Refractive Index Changes.

| Refractive index | RPF | FWHM [THz] | Sensitivity [THz/RIU] | FOM | Q-factor |
|---|---|---|---|---|---|
| 1 | 8.015 | 0.392 | - | - | 20.446 |
| 1.1 | 7.924 | 0.394 | 0.91 | 2.309 | 20.111 |
| 1.2 | 7.888 | 0.396 | 0.36 | 0.909 | 19.919 |
| 1.3 | 7.708 | 0.394 | 1.8 | 4.568 | 19.563 |
| 1.4 | 7.677 | 0.400 | 0.31 | 0.775 | 19.192 |
| 1.5 | 7.572 | 0.401 | 1.05 | 2.678 | 18.882 |

**Table 4**
Analysis of Sensor Response Variations in Mode ***4*** Induced by Refractive Index Changes.

| Refractive index | RPF | FWHM [THz] | Sensitivity [THz/RIU] | FOM | Q-factor |
|---|---|---|---|---|---|
| 1 | 11.44 | 0.334 | - | - | 34.251 |
| 1.1 | 11.310 | 0.333 | 1.3 | 3.903 | 33.963 |
| 1.2 | 11.239 | 0.331 | 0.71 | 2.145 | 33.954 |
| 1.3 | 11.015 | 0.326 | 2.24 | 6.87 | 33.788 |
| 1.4 | 10.951 | 0.328 | 0.64 | 1.951 | 33.387 |
| 1.5 | 10.783 | 0.318 | 1.68 | 5.283 | 33.908 |

as a complementary theoretical framework to describe and interpret the resonance behavior observed in the full-wave simulations.

The results obtained from the Coupled Mode Theory (CMT) are presented below, which clearly demonstrate the good agreement between the full-wave simulation results and those derived from this theoretical approach. The values of the two parameters, $\delta$ and $\gamma_e$, used in the formula for calculating the absorption curve based on the Coupled Mode Theory (CMT) (as shown below), were obtained from a Lorentzian fitting procedure, which is fully described in Reference [3,67]. Since critical coupling occurs at the resonance frequency, the values of these two parameters become equal at 5.29, 6.66, 8.02, and 11.44 THz. The value of $\gamma_e$ and $\delta$ for each frequency are: $\gamma_{e1}= 3 \times 10^{11}$, $\gamma_{e2}= 4 \times 10^{11}$, $\gamma_{e3}= 3 \times 10^{11}$, $\gamma_{e4}= 3.5 \times 10^{11}$, $\delta_1= 3 \times 10^{11}$, $\delta_2= 4 \times 10^{11}$, $\delta_3= 3 \times 10^{11}$, $\delta_4= 3.5 \times 10^{11}$.

$$A = \sum_{i=0}^{N} \left( \frac{4(\gamma_e(i)\delta(i))}{(\omega - \omega(i))^2 + (\gamma_e(i) + \delta(i))^2} \right) \quad (12)$$

The full-wave simulations were compared with the predictions of the coupled-state theory, the two sets of results showed an impressively close match, as illustrated in Fig. 11. To evaluate its effectiveness, Table 5 compares how this sensor performs relative to those developed in earlier research.

As shown in Table 5, the proposed sensor achieves a well-balanced trade-off among key performance metrics. While some previous studies, such as [70] and [76], report much higher Q-factors, they often operate in a single-band regime or exhibit lower sensitivity. In contrast, although Ref. [72] demonstrates higher sensitivity, our design provides quad-band operation (at 5.29, 6.66, 8.02, and 11.44 THz) with high

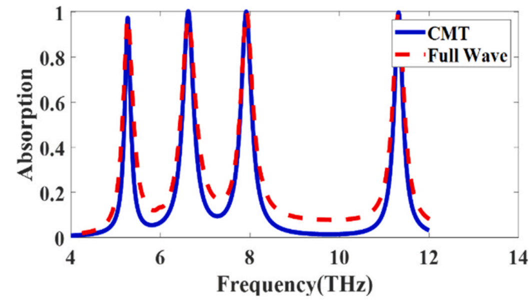


**Fig. 11.** Assessment of agreement between the circuit model and simulation outcomes.

**Table 5**
Comparative table of specifications for refractive index sensors presented in the recent research versus the proposed sensor.

| Ref. | Year | Frequency Range [THz] | Sensitivity [THz/RIU] | FOM | Q-factor |
|---|---|---|---|---|---|
| [70] | 2019 | 3.82 | 0.16 | 62.81 | 1432 |
| [71] | 2019 | 0.8–1.2 | 0.28 | NR | NR |
| [72] | 2019 | 5–15 | 22.720 | 34.96 | 14.32 |
| [73] | 2020 | 2.1–6.25 | 1.57 | 11.75 &24.5 | 40.1 &80 |
| [74] | 2020 | 0.4–2.5 | 0.5 | 15 | NR |
| [75] | 2020 | 0.1–1.9 | 0.28 | 8.54 | 30.5 |
| [76] | 2021 | 1–2 | 1.84 | NR | 277.8 |
| [77] | 2021 | 1–2.4 | 0.152 | 1.5 | 106 |
| [78] | 2022 | 2.5–4.5 | 1.6498 | NR | 11.33 |
| [79] | 2023 | 1.3 | 0.473 | 16.9 | NR |
| [80] | 2024 | 3.24 | 0.726 | 2.69 | NR |
| [81] | 2025 | 2.5 | 0.42 | 1.27 | 5.45 |
| [38] | 2025 | 3–7 | 2.22 | 7.7 | 14.5 |
| This work | 2026 | 4–12 | 1.314 | 4.030 | 33.708 |

NR: not reported

absorption levels (all above 96%). Increasing the number of resonance modes typically complicates the design and, due to increased losses and modal overlap, may reduce the Q-factor. Nevertheless, our structure maintains a competitive sensitivity of 1.314 and an acceptable Q-factor of 33.708 across four distinct bands, making it more versatile for refractive index sensing than single-band, high-Q alternatives.

## 6. Conclusions

This study presents the design and analysis of a plasmonic sensor composed of crossed graphene ribbons. The graphene ribbons are placed on a gold layer, with SiO2 used as a dielectric spacer between them. The structure's performance in simultaneously identifying four frequency bands demonstrates its efficiency in accurately analyzing environmental parameters, including refractive index. The simulation analysis shows that the sensor reaches a sensitivity of 1314 GHz/RIU and provides a Q-factor of 33.708, demonstrating its effective sensing performance. This proposed model can enhance the performance of optical sensors and create new opportunities for applications in refractive index sensing and terahertz communications.

## CRediT authorship contribution statement

**Mohadese Imani:** Writing – original draft, Software, Investigation, Data curation. **Seyed Amin Khatami:** Validation, Project administration. **Shiva Khani:** Writing – review & editing, Validation. **Mohammad Danaie:** Writing – review & editing, Validation, Supervision, Project administration, Conceptualization.

## Ethical approval

The authors confirm that the submitted paper has not been submitted to any other journal and that this version is original and has not been published elsewhere. Additionally, all listed authors affirm the integrity of the study, data, information, and analyses, ensuring that no manipulations have been made. Furthermore, we confirm that no other individuals meet the authorship criteria for this paper beyond those listed as authors.

## Declaration of Generative AI and AI-assisted technologies in the writing process

The authors declare that AI tools were used to improve the English content of this paper.

## Funding

The authors declare that no funds, grants, or financial support were received for the preparation of this manuscript.

## Declaration of Competing Interest

The authors declare that they have no known competing financial interests or personal relationships that could have appeared to influence the work reported in this paper.

## Data availability

Data will be made available on request.

## References

[1] S. Zhou, K. Bi, Q. Li, L. Mei, Y. Niu, W. Fu, S. Han, S. Zhang, J. Mu, L. Tan, W. Geng, Patterned graphene-based metamaterials for terahertz wave absorption, Coatings 13 (1) (2022 Dec 29) 59.
[2] L. Li, F. Chen, Tunable four-band metamaterial absorber and sensor based on a anastacking double-ring Dirac semimetal structure design, Phys. Lett. A 544 (2025 Jun 5) 130489.
[3] H. Fu, F. Chen, Dual-narrowband terahertz absorber with independently tunable amplitude and frequency: a theoretical study, Phys. Lett. A (2026 Jan 21) 131395.
[4] S. Koenig, D. Lopez-Diaz, J. Antes, F. Boes, R. Henneberger, A. Leuther, A. Tessmann, R. Schmogrow, D. Hillerkuss, R. Palmer, T. Zwick, Wireless sub-THz communication system with high data rate, Nat. Photonics 7 (12) (2013 Dec) 977–981.
[5] Y. Wang, S. Cheng, B. Li, C. Tang, F. Gao, Y. Yi, Mid-infrared high-sensitivity four-peak graphene absorber based on circular ring-nested ellipses: Polarization-independent characteristics and dynamic tunability, Physica E Low-dimensional Systems Nanostructures (2026 Mar 27) 116523.
[6] Bhishma Karki, Youssef Trabelsi, Rajeev Kumar, Subbulakshmi Ganesan, Alok Kumar Mishra, T. Krithiga, Sanjeev Kumar, Effect of thallium bromide and gold layer thickness on the optical performance of surface plasmon resonance sensors, Physica B Condensed Matter 717 (2025) 417803, https://doi.org/10.1016/j.physb.2025.417803.
[7] Bhishma Karki, Abdullah Saad Alsubaie, Rajeev Kumar, M. Sudhakara Reddy, Joany R. M, Hemanta Kumar Palo, Sanjeev Kumar, Enhanced surface plasmon resonance sensing using MXene and tantalum disulfide-based multilayer structures, Surf. Interfaces 80 (2026) 108409, https://doi.org/10.1016/j.surfin.2025.108409.
[8] R. Nasirifar, M. Danaie, A. Dideban, Hollow-core graded index optical fiber refractive index sensor based on surface plasmon resonance, Opt. & Quantum Electron. 52 (7) (2020 Jul 1) 1.
[9] N. Korani, S. Mohammadi, A. Hocini, M. Danaie, Smith chart–based impedance matching and chirality analysis of an ultra-broadband plasmonic graphene absorber for sensing applications, Results Eng. (2026 May 20) 111168.
[10] A.K. Kaveev, G.I. Kropotov, Physical principles of filtration and the design of terahertz radiation filters, Uspekhi Fiz. Nauk. 196 (2) (2026 Feb 1) 182–204.
[11] G.C. Ram, A.B. Jambek, M.V. Subbarao, D.R. Varma, M.V. Rao, N.K. Maurya, K. B. Sindhuri, A reconfigurable graphene–VO2 based terahertz bandpass filter for differential sensing and ML-based refractive index prediction, Physica B Condensed Matter (2026 Jun 9) 418886.
[12] X. Ma, H. Tian, Y. Wen, J. Song, B. Wang, Broadband and high-pass filtering based on city-wall-shaped MIM waveguide structure, Opt. Commun. (2026 Mar 26) 133190.
[13] N. Korani, S. Mohammadi, A. Hocini, M. Danaie, A terahertz tunable plasmonic absorber based on step-shaped graphene patches for sensing applications, Plasmonics 20 (8) (2025 Aug) 6725–6738.
[14] M. Kehtarmanesh, P. Keshavarzi, M. Danaie, Design of non-volatile plasmonic memory using phase-change material as a neuromorphic synapse, Opt. Quantum Electron. 58 (10) (2026) 430.
[15] O. Sharifipour, P. Keshavarzi, M. Danaie, Ultra-compact all-optical plasmonic switch with triangular resonator and phase-change materials for neuromorphic and advanced optical networks, Opt. Commun. 591 (2025 Oct 1) 132101.
[16] E. Adibnia, Deep Reinforcement Learning-Based Optimization of Identical-Dual-Band Filters, IEEE Trans. Neural Netw. Learn. Syst. (2026 May) 1.
[17] M. Shooshtari, T. Serrano-Gotarredona, B. Linares-Barranco, Review of memristors for in-memory computing and spiking neural networks, Adv. Intell. Syst. 8 (3) (2026 Mar) e202500806.
[18] N. Melouki, H. Nasseri, A. Iqbal, T.A. Denidni, Compact quarter-mode SIW self-triplexing antenna for C-band and X-band applications. In2023 17th European Conference on Antennas and Propagation (EuCAP), IEEE, 2023 Mar 26, pp. 1–5.
[19] R. Rahad, A.S. Mohsin, M.B. Bhuian, M.M. Rahman, Graphene-metamaterial based tunable broadband polarization insensitive absorber for terahertz antenna design, Ieee Access. 12 (2024 Apr 2) 48654–48667.
[20] S. Liang, F. Xu, W. Li, W. Yang, S. Cheng, H. Yang, J. Chen, Z. Yi, P. Jiang, Tunable smart mid infrared thermal control emitter based on phase change material VO2 thin film, Appl. Therm. Eng. 232 (2023 Sep 1) 121074.
[21] S. Liang, S. Cheng, H. Zhang, W. Yang, Z. Yi, Q. Zeng, B. Tang, P. Wu, S. Ahmad, T. Sun, Structural color tunable intelligent mid-infrared thermal control emitter, Ceram. Int. 50 (13) (2024 Jul 1) 23611–23620.
[22] W. Li, W. Zhao, S. Cheng, H. Zhang, Z. Yi, T. Sun, P. Wu, Q. Zeng, R. Raza, Tunable metamaterial absorption device based on Fabry–Perot resonance as temperature and refractive index sensing, Opt. Lasers Eng. 181 (2024 Oct 1) 108368.
[23] W. Li, Y. Liu, L. Ling, Z. Sheng, S. Cheng, Z. Yi, P. Wu, Q. Zeng, B. Tang, S. Ahmad, The tunable absorber films of grating structure of AlCuFe quasicrystal with high Q and refractive index sensitivity, Surf. Interfaces 48 (2024 May 1) 104248.
[24] Y. Zheng, W. Zhao, Q. Song, C. Ma, Z. Yi, Q. Zeng, T. Sun, J. Chen, J. Yan, Analysis of solar absorption and thermal radiation properties of a multi-layer structure, Int. J. Therm. Sci. 203 (2024 Sep 1) 109172.
[25] Z. Yi, J. Huang, C. Cen, X. Chen, Z. Zhou, Y. Tang, B. Wang, Y. Yi, J. Wang, P. Wu, Nanoribbon-ring cross perfect metamaterial graphene multi-band absorber in THz range and the sensing application, Results Phys. 14 (2019 Sep 1) 102367.
[26] M. Alsharari, B.B. Han, K. Aliqab, A. Flah, A. Armghan, Y. Sharma, S.K. Patel, Highly efficient graphene-based gold-ceramic material surface plasmon resonance biosensor: An artificial intelligence optimization for detecting organic compounds, Mater. Today Adv. 31 (2026 Aug 1) 100877.
[27] M. Khafagy, A.M. Ghanim, M.A. Swillam, Tunable multi-band terahertz sensor based on graphene plasmonic metasurfaces, Sci. Rep. 16 (1) (2026 Feb 11) 5938.
[28] J. Valentine, S. Zhang, T. Zentgraf, E. Ulin-Avila, D.A. Genov, G. Bartal, X. Zhang, Three-dimensional optical metamaterial with a negative refractive index, nature 455 (7211) (2008 Sep 18) 376–379.
[29] B.J. Pendry, Metamaterials and negative refraction, Nat. Mater. 5 (2006) 755–764.
[30] X. Luo, X. Zhai, L. Wang, Q. Lin, Enhanced dual-band absorption of molybdenum disulfide using a plasmonic perfect absorber, Opt. Express 26 (9) (2018 Apr 20) 11658–11666.
[31] L. Jylhä, I. Kolmakov, S. Maslovski, S. Tretyakov, Modeling of isotropic backward-wave materials composed of resonant spheres, J. Appl. Phys. 99 (4) (2006 Feb 15).
[32] X. Zhao, X. Ren, Y. Yang, J. Bai, Y. Zheng, J. Chen, C. Xue, High-temperature refractive index sensor with high sensitivity and wide measurement range based on the fiber open Fabry-Pérot interferometer, Opt. Express 33 (17) (2025 Aug 11) 35200–35210.
[33] M. Mishra, M. Sharma, M. Goyal, B. Singh, Plasmonic ring resonator for biosensing and integrated photonics, Mod. Phys. Lett. B 39 (36) (2025 Dec 30) 2550249.
[34] P. Karami, F. Parandin, Design of an ultrasensitive and thermally stable 2D photonic crystal biosensor for early detection of breast cancer cells in lymph nodes, Measurement 270 (2026 Apr 21) 120889.
[35] S. Anwar, M. Khan, High-performance terahertz refractive index sensor for cancer cells detection, Eur. Phys. J. E 46 (3) (2023 Mar) 19.
[36] C. Cen, Z. Yi, G. Zhang, Y. Zhang, C. Liang, X. Chen, Y. Tang, X. Ye, Y. Yi, J. Wang, J. Hua, Theoretical design of a triple-band perfect metamaterial absorber in the THz frequency range, Results Phys. 14 (2019 Sep 1) 102463.
[37] M.Z. Riaz, S. Ahmed, H. Chen, Q. Qin, High Q-factor fano resonance via coupling of topological corner states and waveguides for enhanced optical sensing, Opt. & Laser Technol. 192 (2025 Dec 1) 113845.
[38] S.A. Khatami, P. Rezaei, M. Danaie, Early diagnosis of breast cancer with a highly accurate dual-band graphene-based refractive index sensor, J. Adv. Dielectr. 16 (03) (2026 Jun 31) 2550040.
[39] S.K. Khandare, K. Allabouche, N.E. El Idrissi, A compact broadband polarization-diverse 1× 2 slotted graphene antenna array on a $SiO_2$ for terahertz devices, Phys. Lett. A (2026 Apr 25) 131732.
[40] R. Mahapatra, T. Raj, D. Kumar, S. Kundu, Graphene-Based Compact Ultrawideband Terahertz Plasmon Antenna With Characteristic Mode Analysis, IEEE Trans. Plasma Sci. (2026 Mar 12).
[41] Q. Wang, B. Li, L. Zeng, Q. Yang, X. Zhang, R. Wen, C. Deng, Switchable quadruple narrowband to broadband terahertz perfect absorber based on graphene and VO2 metamaterials, Diam. Relat. Mater. 142 (2024 Feb 1) 110832.
[42] G. Li, Tunable Fano resonance for advanced sensing in graphene-based metasurface, Diam. Relat. Mater. 142 (2024 Feb 1) 110823.
[43] W. Li, M. Liu, S. Cheng, H. Zhang, W. Yang, Z. Yi, Q. Zeng, B. Tang, S. Ahmad, T. Sun, Polarization independent tunable bandwidth absorber based on single-layer graphene, Diam. Relat. Mater. 142 (2024 Feb 1) 110793.
[44] Y. Chen, G. Duan, C. Xu, X. Qin, Q. Zhao, H. Zhou, B.X. Wang, Triple-band graphene-based tunable electromagnetically induced transparency terahertz

metamaterial with multi-frequency optical switching, Diam. Relat. Mater. 143 (2024 Mar 1) 110939.
[45] L. Jiang, C. Yuan, Z. Li, J. Su, Z. Yi, W. Yao, P. Wu, Z. Liu, S. Cheng, M. Pan, Multi-band and high-sensitivity perfect absorber based on monolayer graphene metamaterial, Diam. Relat. Mater. 111 (2021 Jan 1) 108227.
[46] W. Lu, Z. Yi, J. Zhang, X. Xu, B. Tang, G. Li, L. Zeng, J. Chen, T. Sun, A tunable broadband absorber in the terahertz band based on the proportional structure of a single layer of graphene, Diam. Relat. Mater. 140 (2023 Dec 1) 110481.
[47] H. Zhang, Z. Chen, Z. Yi, S. Cheng, S. Ahmad, C. Tang, J. Deng, Three band THz perfect absorption device based on graphene metasurface structure, Physica E Low-dimensional Systems Nanostructures (2026 Apr 4) 116542.
[48] A.R. Jalalvand, Z. Rashidi, M. Khajenoori, Sensitive and selective simultaneous biosensing of nandrolone and testosterone as two anabolic steroids by a novel biosensor assisted by second-order calibration, Steroids 189 (2023 Jan 1) 109138.
[49] H. Bensalah, A. Hocini, H. Bahri, D. Khedrouche, S. Ingebrandt, V. Pachauri, A plasmonic refractive index sensor with high sensitivity and its application for temperature and detection of biomolecules, J. Opt. 52 (3) (2023 Sep) 1035–1046.
[50] S. Vidhya, J. Wekalao, G.R. Reddy, AI-Enhanced glucose detection using a circular based SPR biosensor with Graphene-Mxene-Au-Architecture, Plasmonics 21 (1) (2026 Jan) 761–772.
[51] Z. Salehnezhad, M. Soroosh, A. Farmani, Design and numerical simulation of a sensitive plasmonic-based nanosensor utilizing MoS2 monolayer and graphene, Diam. Relat. Mater. 131 (2023 Jan 1) 109594.
[52] A.M. Tuaimah, H.J. Taher, S.R. Tahhan, F.A. Al-Zahrani, K. Ahmed, Plasmonic D-shaped bimetallic coating refractive index sensor, Plasmonics 18 (6) (2023 Dec) 2393–2404.
[53] H. Mathuriya, R. Zafar, G. Singh, Plasmonic grating-based refractive index sensor with high sensitivity, IETE J. Res. 69 (6) (2023 Aug 18) 3661–3667.
[54] Q. Shangguan, Y. Zhao, Z. Song, J. Wang, H. Yang, J. Chen, C. Liu, S. Cheng, W. Yang, Z. Yi, High sensitivity active adjustable graphene absorber for refractive index sensing applications, Diam. Relat. Mater. 128 (2022 Oct 1) 109273.
[55] Y. Zha, S. Cheng, Tunable high-sensitivity mid-infrared perfect absorber with five resonance peaks based on nested circular and elliptical ring graphene surface plasmons, Physica B Condensed Matter (2026 Jun 9) 418929.
[56] Y. Wang, S. Cheng, B. Li, C. Tang, F. Gao, Y. Yi, Mid-infrared high-sensitivity four-peak graphene absorber based on circular ring-nested ellipses: Polarization-independent characteristics and dynamic tunability, Physica E Low-dimensional Systems Nanostructures (2026 Mar 27) 116523.
[57] Z. Chen, M. Liu, S. Cheng, J. Wang, Y. Yi, B. Li, C. Tang, F. Gao, Bilayer graphene metasurface fo dynamically reconfigurable terahertz perfect absorption, Curr. Appl. Phys. (2025 Oct 2).
[58] Z. Jin, M. Liu, S. Cheng, Z. Yi, J. Wang, B. Li, Broadband tunable metasurface absorbing device in the terahertz band based on single-layer graphene, Mod. Phys. Lett. B 40 (06) (2026 Feb 28) 2650017.
[59] Y. Xing, F. Chen, Tunable terahertz broadband absorber based on single-layer pattern, Micro Nanostruct. (2026 May 23) 208759.
[60] L. Li, F. Chen, W. Yang, Dual-parameters tunable broadband THz absorber using hybrid graphene-Dirac Semimetal metamaterial structure, Physica B Condensed Matter 728 (2026 Apr 15) 418358.
[61] Y. Li, F. Chen, W. Yang, A multifunctional bidirectional metamaterial perfect absorber for efficient narrowband and broadband absorption, Opt. Commun. 586 (2025 Aug 1) 131878.
[62] H. Fu, F. Chen, W. Yang, A broadband absorber based on W− TiO2 ellipsoidal core-shell array structure, Physica B Condensed Matter 705 (2025 May 15) 417077.
[63] T.Y. Zeng, G.D. Liu, L.L. Wang, Q. Lin, Light-matter interactions enhanced by quasi-bound states in the continuum in a graphene-dielectric metasurface, Opt. Express 29 (24) (2021 Nov 16) 40177–40186.
[64] N. Shiraishi, J. Lu, F.B. Fauzi, R. Imaizumi, T. Tsukahara, S. Mogari, S. Iida, Y. Matsukura, S. Teramoto, K. Yokoi, I. Ichinose, Basic Characteristics of Ionic Liquid-Gated Graphene FET Sensors for Nitrogen Cycle Monitoring in Agricultural Soil, Biosensors 15 (1) (2025 Jan 16) 55.
[65] S. Zhang, H. Yang, C. Tang, Z. Yi, J. Zhang, J. Wang, B. Li, Multiple tunable six-peak graphene absorber for high-performance refractive index sensing, Physica B Condensed Matter 708 (2025 Jul 1) 417225.
[66] H. Ma, P. Shi, Z. Yi, A Highly Sensitive Graphene-Based Terahertz Perfect Absorber Featuring Five Tunable Absorption Peaks, Materials 18 (11) (2025 Jun 3) 2601.
[67] S.A. Khatami, P. Rezaei, Coupled mode theory analysis of the graphene-based multi-band superabsorber for selective sensing application, Diam. Relat. Mater. (2025 Jul 31) 112690.
[68] E.P. de Santana, K.T. Wang, S. Abadal, D. Stock, Z. Wang, A.K. Wigger, E. Alarcón, M.C. Lemme, P.H. Bolívar, A THz graphene-on-hBN stack patch antenna for future 6G communications, Sci. Rep. 15 (1) (2025 Sep 23) 32650.
[69] G.W. Hanson, Dyadic Green's functions and guided surface waves for a surface conductivity model of graphene, J. Appl. Phys. 103 (6) (2008 Mar 15).
[70] F.G. Vanani, A. Fardoost, R. Safian, Design of double ring label-free terahertz sensor, IEEE Sens. J. 19 (4) (2018 Nov 14) 1293–1298.
[71] Y.K. Srivastava, R.T. Ako, M. Gupta, M. Bhaskaran, S. Sriram, R. Singh, Terahertz sensing of 7 nm dielectric film with bound states in the continuum metasurfaces, Appl. Phys. Lett. 115 (15) (2019 Oct 7).
[72] M. Nejat, N. Nozhat, Ultrasensitive THz refractive index sensor based on a controllable perfect MTM absorber, IEEE Sens. J. 19 (22) (2019 Jul 25) 10490–10497.
[73] E. Rezagholizadeh, M. Biabanifard, S. Borzooei, Analytical design of tunable THz refractive index sensor for TE and TM modes using graphene disks, J. Phys. D Appl. Phys. 53 (29) (2020 Jul 15) 295107.
[74] Y. Wang, D. Zhu, Z. Cui, L. Yue, X. Zhang, L. Hou, K. Zhang, H. Hu, Properties and sensing performance of all-dielectric metasurface THz absorbers, IEEE Trans. Terahertz Sci. Technol. 10 (6) (2020 Jul 17) 599–605.
[75] T. Chen, D. Zhang, F. Huang, Z. Li, F. Hu, Design of a terahertz metamaterial sensor based on split ring resonator nested square ring resonator, Mater. Res. Express 7 (9) (2020 Sep 1) 095802.
[76] X. Du, F. Yan, W. Wang, L. Zhang, Z. Bai, H. Zhou, Y. Hou, Thermally-stable graphene metamaterial absorber with excellent tunability for high-performance refractive index sensing in the terahertz band, Opt. & Laser Technol. 144 (2021 Dec 1) 107409.
[77] Z. Li, Z. Yi, T. Liu, L. Liu, X. Chen, F. Zheng, J. Zhang, H. Li, P. Wu, P. Yan, Three-band perfect absorber with high refractive index sensing based on an active tunable Dirac semimetal, Phys. Chem. Chem. Phys. 23 (32) (2021) 17374–17381.
[78] M.Y. Azab, M.F. Hameed, A.M. Nasr, S.S. Obayya, Highly sensitive metamaterial biosensor for cancer early detection, IEEE Sens. J. 21 (6) (2021 Jan 12) 7748–7755.
[79] Barzegar-Parizi S. Refractive index sensor with dual sensing bands based on array of Jerusalem cross cavities to detect the hemoglobin concentrations, Opt. & Quantum Electron. 55 (1) (2023 Jan 1) 1.
[80] S.A. Khatami, P. Rezaei, M. Danaie, High accuracy graphene-based refractive index sensor: analytical approach, Diam. Relat. Mater. 146 (2024 Jun 1) 111225.
[81] S.A. Khatami, P. Rezaei, P. Zamzam, S. Hadipour, S. Khani, Smith chart analysis for transmission line method validation of a simple graphene-based absorber in sugar molecules detection, Results Phys. (2025 Sep 25) 108464.